USC-SIPI REPORT #197

Shape Reconstruction From Photometric Stereo

by

Kyoung Mu Lee and C.-C. Jay Kuo

February 1992

Signal and Image Processing Institute
UNIVERSITY OF SOUTHERN CALIFORNIA
Department of Electrical Engineering-Systems
Electrical Engineering Building
University Park/MC-2564
Los Angeles, CA 90089 U.S.A.

Submitted to Journal of the Optical Society of America A

Shape Reconstruction From Photometric Stereo*

Kyoung Mu Lee[†] and C.-C. Jay Kuo [†]

February 10, 1992

Abstract

Two new iterative algorithms for shape reconstruction based on multiple images taken under different lighting conditions known as photometric stereo are proposed. In our previous work, an iterative SFS (Shape From Shading) algorithm using a single image was developed by combining a triangular element surface model with a linearized reflectance map. It is shown in this research that all single-image SFS algorithms share an inherent problem, i.e. the accuracy of the reconstructed surface height is related to the slope of the reflectance map function defined on the gradient space. This observation motivates us to generalize the single-image SFS algorithm to two photometric stereo SFS algorithms aiming at more accurate surface reconstruction. The two algorithms directly determine the surface height by minimizing a quadratic cost functional, which is defined to be the squares of the brightness error obtained from each individual image in a parallel or cascade manner. The optimal illumination condition which leads to best shape reconstruction is also derived. Simulation results for several test images are given to demonstrate the performance of our new algorithms.

1 Introduction

Extracting the surface information of an object from its shaded image, known as the shape from shading (SFS) problem, is one of the fundamental problems in computer vision. The image formation process consists of three factors: the object shape, the property of object surface and the illumination condition (light source information). If the surface property and the lighting condition are known a priori, the shading information provides important cues for 3-D surface reconstruction since the variation in brightness arises primarily due to the change in surface orientation. Research on the SFS problem has been performed

---

*This work was supported by a National Science Foundation Research Initiation Award (ASC-9009323).

[†] The authors are with the Signal and Image Processing Institute and the Department of Electrical Engineering-Systems, University of Southern California, Los Angeles, California 90089-2564. E-mail: kyoungmu@sipi.usc.edu and cckuo@sipi.usc.edu. Phone: (213) 740-4658; Fax: (213) 740-4651

extensively in the last two decades. Many SFS algorithms using a single image have been developed such as the characteristic strip method [2], [3], the variational method [1], [4], [5], [7], [10], [17], [18], [19], [26] and Fourier method [13]. It is well known that this problem is ill-posed so that the solution may not be reliable. Thus, researchers have also considered the use of multiple images to provide additional information for robust surface reconstruction, which includes the photometric stereo method [9], [6], [14], [16], [20], [23], [24], [25] and the geometric stereo method [12].

The photometric stereo method was first proposed by Woodham [23], [24], [25] and has been studied and extended for practical implementation by several researchers [9], [6], [14], [16], [20]. With this method, one uses images taken from the same viewing direction under different lighting conditions. The surface orientation of a local point is determined by its irradiances in these images by using the fact the orientation corresponds to the intersection of constant brightness contours of different reflectance maps on the gradient space. One special feature of Woodham's method is that it is a local method where the surface orientation is determined point by point. Thus, it is applicable without the smooth surface and the constant albedo constraints. In contrast, the single-image SFS problem cannot be solved locally since there is no sufficient constraint at a local point. Some global properties such as the smooth surface assumption have to be incorporated to regularize the problem.

In this research, we provide a unifying approach to solve both single-image and photometric stereo SFS problems. Our new approach is based on the single-image SFS algorithm proposed in [11]. We show that the single-image SFS algorithm may not yield an accurate result by examining the characteristics of the reflectance map, and explain how to use the photometric stereo information to improve the accuracy of the reconstructed surface. We propose two SFS algorithms using photometric stereo images and call them the parallel and cascade schemes. The parallel scheme combines the information of all images simultaneously while the cascade scheme uses the information of each image in sequence. Both schemes are formulated as a quadratic functional minimization problem parameterized by surface heights, where the cost functional is defined to be the squares of the brightness error. The surface heights can be obtained by solving the equivalent large sparse linear system of equations with efficient linear system solvers such as the multi-grid (MG) or the preconditioned conjugate gradient (PCG) method. The optimal illumination condition which leads to best shape reconstruction is also discussed in the current setting and verified experimentally.

Compared to the conventional photometric stereo method, our new method have two major advantages. First, the new method determines surface heights directly while the conventional photometric stereo method determines only the surface orientations. Thus, the integrability problem arises in the conventional method but not in ours. Second, the new method is a global method which minimizes the squared intensity errors over all points so that it is insensitive to the noise. In contrast, the conventional one is a local method and is more sensitive to the noise. However, it is worthwhile to point out that our method requires the smooth surface constraint while the conventional method does not.

2 Conventional Photometric Stereo

Under the assumption of orthographic projection, Lambertian surface and a distant single point light source, the reflectance map is basically a function characterizing the relationship between the image irradiance and the orientation of the object surface. It can be derived that

$$R(p,q) = \begin{cases} \eta \mathbf{l}^T \mathbf{n}, & \mathbf{l}^T \mathbf{n} \geq 0, \\ 0, & \mathbf{l}^T \mathbf{n} < 0, \end{cases} \tag{2.1}$$

where η is the albedo of the surface,

$$\mathbf{n} = \frac{(-p,-q,1)^T}{\sqrt{1+p^2+q^2}}$$

is the surface normal, and

$$\mathbf{l} = (\cos\tau \sin\sigma, \sin\tau \sin\sigma, \cos\sigma)^T$$

is the unit vector of the illumination direction pointing toward the light source, and where τ and σ are the *tilt* and *slant* angles that the illumination direction makes with x and z axis, respectively. This can be also represented as

$$\mathbf{l} = \frac{(-p_s,-q_s,1)^T}{\sqrt{1+p_s^2+q_s^2}},$$

where p_s and q_s denote the slope of a surface element perpendicular to the illumination direction.

Substituting the vectors $\mathbf{n}$ and $\mathbf{l}$ into (2.1), we obtain

$$R(p,q) = \begin{cases} \eta \frac{K}{\sqrt{1+p^2+q^2}}, & K \geq 0, \\ 0, & K < 0, \end{cases} \tag{2.2a}$$

where

$$K = -p\cos\tau\sin\sigma - q\sin\tau\sin\sigma + \cos\sigma,$$

or equivalently,

$$R(p,q) = \begin{cases} \eta\frac{1+p_sp+q_sq}{\sqrt{(1+p^2+q^2)}\sqrt{(1+p_s^2+q_s^2)}}, & 1+p_sp+q_sq \geq 0, \\ 0, & 1+p_sp+q_sq < 0. \end{cases} \tag{2.2b}$$

The reflectance map $R(p,q)$ is a nonlinear function which can be depicted as nested contours in the gradient space (p,q). The basic equation for the image formation process can therefore be expressed as

$$E(x,y) = R(p,q), \tag{2.3}$$

which is known as the *image irradiance equation.*

Conventional photometric stereo is an algebraic method to solve the image irradiance equation. With given albedo η, illumination direction $\mathbf{l}$ and image irradiance E, there are two unknown variables p and q in (2.3) so that at least two equations are needed to determine the values of p and q. However, since (2.3) is nonlinear, it may have more than one solution and a third image is often needed to form an overdetermined system.

Based on the reflection map (2.1), we can provide a simple viewpoint to understand the solution procedure. Suppose that we have three images obtained with illumination directions $\mathbf{l}_1, \mathbf{l}_2$, and $\mathbf{l}_3$. At a given point (x,y), the observed image irradiances in these three images are E_1, E_2 and E_3, respectively. Thus, we have three image irradiance equations

$$E_i = \eta\mathbf{l}_i^T\mathbf{n}, \quad i = 1,2,3,$$

where $\mathbf{n}$ is the surface normal at the point (x,y). These equations can be written in matrix form as

$$\mathbf{E} = \eta\mathbf{L}\mathbf{n}, \tag{2.4}$$

where

$$\mathbf{E} = \begin{pmatrix} E_1 \\ E_2 \\ E_3 \end{pmatrix}, \quad \text{and} \quad \mathbf{L} = \begin{pmatrix} \mathbf{l}_1^T \\ \mathbf{l}_2^T \\ \mathbf{l}_3^T \end{pmatrix}.$$

If $\mathbf{l}_1, \mathbf{l}_2$, and $\mathbf{l}_3$ are linearly independent, $\mathbf{L}^{-1}$ exists and (2.4) can be solved for $\mathbf{n}$. However, note that the surface normal $\mathbf{n}$ is a unit vector with two free variables. Thus, (2.4) is an overdetermined system and we may obtain its least squares solution.

One feature of the above formulation is that it applies nicely if the albedo η is not known a priori and varying at different image points. That is, we know from (2.4) that

$$\eta \mathbf{n} = \mathbf{L}^{-1}\mathbf{E}. \tag{2.5}$$

The magnitude of the right hand side of (2.5) gives the value of albedo at (x, y),

$$\eta = \|\mathbf{L}^{-1}\mathbf{E}\|,$$

and the corresponding unit surface normal **n** is

$$\mathbf{n} = \frac{1}{\eta}\mathbf{L}^{-1}\mathbf{E}.$$

3 Single-Image SFS Using a Triangular Element Surface Model

Recently, we [11] developed a new iterative algorithm that recovers surface heights directly by combining a triangular element surface model with a successively linearized reflectance map. The key idea is to approximate a smooth surface by the union of triangular surface patches called triangular elements, and express the approximating surface as a linear combination of a set of nodal basis functions. Since the surface normal of a triangular element is uniquely determined by the heights of its three vertices (or nodes), the image brightness can be directly related to the nodal heights via the nonlinear reflectance map function. To simplify the solution procedure, the reflectance map is linearized at each iteration so that the surface height can be determined by minimizing a quadratic cost functional corresponding to the squares of the brightness error. The minimization problem is then solved effectively with the multigrid computational technique.

By taking the Taylor series expansion of $R(p, q)$ about a certain reference point (p_0, q_0) through the first-order term, we have the linear approximation of the reflectance map as follows

$$R(p,q) \approx R(p_0,q_0) + (p - p_0)\frac{\partial R(p,q)}{\partial p}\Big|_{(p_0,q_0)} + (q - q_0)\frac{\partial R(p,q)}{\partial q}\Big|_{(p_0,q_0)}. \tag{3.1}$$

The reference point (p_0, q_0) can be either fixed or varying for different values of (p, q).

Consider the approximation of a smooth surface with a union of triangular surface patches over a uniform grid domain as illustrated in Fig. 1 [8], [15]. The approximating surface can be expressed as a linear combination of basis functions ϕ_i with local compact support known as the finite triangular elements (see Fig. 2) such that

$$z(x,y) = \sum_{i=1}^{M_n} z_i \phi_i(x,y),$$

where z_i is the value of $z(x,y)$ at the ith node and M_n is the number of nodal basis functions. Based on the triangular element surface model, the orientation (i.e. the surface normal vector) of a triangular patch can be determined by the heights of its three vertices (or nodes) in a linear functional form as

$$p(x,y) = \frac{\partial z(x,y)}{\partial x} = \sum_{i=1}^{M_n} z_i \frac{\partial \phi_i(x,y)}{\partial x}, \tag{3.2}$$

and

$$q(x,y) = \frac{\partial z(x,y)}{\partial y} = \sum_{i=1}^{M_n} z_i \frac{\partial \phi_i(x,y)}{\partial y}. \tag{3.3}$$

Combining this surface model with the linearized reflectance map image formation model given by (3.1), we can express the image irradiance directly in terms of nodal heights of triangular elements. By substituting (3.2) and (3.3) into (3.1), we have

$$E = R(p,q) \approx \alpha p + \beta q + \gamma = \sum_{i=1}^{M_n} \Phi_i z_i + \gamma, \tag{3.4}$$

where

$$\Phi_i(x,y) = \alpha \frac{\partial \phi_i(x,y)}{\partial x} + \beta \frac{\partial \phi_i(x,y)}{\partial y}, \qquad \gamma = R(p_0,q_0) - \alpha p_0 - \beta q_0, \tag{3.4a}$$

and

$$\alpha = \frac{\partial R(p,q)}{\partial p}\Big|_{(p_0,q_0)}, \qquad \beta = \frac{\partial R(p,q)}{\partial q}\Big|_{(p_0,q_0)}. \tag{3.4b}$$

To estimate the nodal heights z_i based on the shading information, we consider the cost functional

$$\mathcal{E} = \mathcal{E}_b + \lambda \mathcal{E}_s, \tag{3.5}$$

where $\mathcal{E}_b$ and $\mathcal{E}_s$ denote the cost term due to the brightness error and smoothness constraint, respectively, and λ is the smoothing factor.

The first term can be formulated as the sum of the squared brightness error,

$$\mathcal{E}_b = \iint_{\Omega} (E_o - E)^2 \, dx \, dy, \tag{3.6}$$

where E_o is the observed image irradiance and E is the irradiance generated by the reflectance map model. By substituting (3.4) into (3.6), we obtain

$$\begin{aligned} \mathcal{E}_b &= \iint_\Omega [E_o - (\sum_{i=1}^{M_n} \Phi_i z_i + \gamma)]^2 \, dx \, dy \\ &= \frac{1}{2}\mathbf{z}^T \mathbf{A} \mathbf{z} - \mathbf{b}^T \mathbf{z} + \mathbf{c}, \end{aligned} \tag{3.7}$$

where the elements $a_{i,j}$ and b_i of the stiffness matrix $\mathbf{A}$ and the load vector $\mathbf{b}$ can be computed as

$$a_{i,j} = 2 \iint_\Omega \Phi_i \Phi_j \, dx \, dy, \qquad b_i = 2 \iint_\Omega (E_o - \gamma) \Phi_i \, dx \, dy \qquad 1 \le i, j \le M_n. \tag{3.8}$$

Note that two different triangulation schemes can be made by choosing two different directions of the oblique lines, i.e. 45° and 135°. Let us denote the resulting stiffness matrices and load vectors with 45°- and 135°-triangulation by $\mathbf{A}_r$, $\mathbf{b}_r$ and $\mathbf{A}_l$, $\mathbf{b}_l$, respectively. When the image domain is triangulated with the 45° oblique lines as shown in Fig. 1, there exists a directional preference along the 45° direction, since only six nodal points among the eight nearest neighbors are associated with the central nodal point. The triangulation scheme may sometimes affect the results of the algorithm under various illumination directions. For example, consider a spherically symmetric object illuminate by light sources with tilt angles 45° and 135°, respectively. The reconstructed surfaces will be slightly different due to different triangulations. To avoid the directional preference, we may use two triangulation schemes simultaneously so that the combined stiffness matrix $\mathbf{A}_t$ and load vector $\mathbf{b}_t$ can be computed via

$$\mathbf{A}_t = \frac{1}{2}(\mathbf{A}_r + \mathbf{A}_l), \qquad \mathbf{b}_t = \frac{1}{2}(\mathbf{b}_r + \mathbf{b}_l), \tag{3.9}$$

which is equivalent to the averaging of their individual cost functionals. However, we want to point out that the combination of two triangulation schemes requires extra computational cost. This is especially true for the multi-grid method in which the stiffness matrices have to be computed at every coarse grid level. Although the single triangulation scheme is simpler, numerical experiments show that it often gives satisfactory results.

The smoothness constraint on the reconstructed surface can be imposed by adding an additional term to the cost functional $\mathcal{E}_b$ such as *thin plate* energy model

$$\mathcal{E}_{s,c} = \frac{1}{2} \iint (z_{xx}^2 + 2z_{xy}^2 + z_{yy}^2) \, dx \, dy. \tag{3.10}$$

By discretizing (3.10), we obtain

$$\begin{aligned}\mathcal{E}_s &= \frac{1}{2h^2}\sum_{n_x}\sum_{n_y}[(z_{n_x+1,n_y} - 2z_{n_x,n_y} + z_{n_x-1,n_y})^2 + 2(z_{n_x+1,n_y+1} - z_{n_x,n_y+1} \\ &\qquad - z_{n_x+1,n_y} + z_{n_x,n_y})^2 + (z_{n_x,n_y+1} - 2z_{n_x,n_y} + z_{n_x,n_y-1})^2],\end{aligned}$$

where h is the grid spacing. The above equation can be expressed in matrix form as

$$\mathcal{E}_s = \frac{1}{2}\mathbf{z}^T\mathbf{B}\mathbf{z}, \tag{3.11}$$

where $\mathbf{z}$ is the vector of nodal variables and $\mathbf{B}$ is a sparse symmetric matrix. It is convenient to view the matrix-vector product $\mathbf{B}\mathbf{z}$ as a local nodal operator operating on a 2-D array. The local nodal operator is of the following stencil form

$$\mathbf{B}: \quad \frac{1}{h^2}\left|\begin{array}{ccccc} & & 1 & & \\ & 2 & -8 & 2 & \\ 1 & -8 & 20 & -8 & 1 \\ & 2 & -8 & 2 & \\ & & 1 & & \end{array}\right|.$$

The operator stencils for points near the boundary region have to be treated specially. They are given in [11], [21], [22].

Substituting (3.7) and (3.11) into (3.5), we have the overall cost functional in matrix form as

$$\mathcal{E} = \frac{1}{2}\mathbf{z}^T\mathbf{C}\mathbf{z} - \mathbf{b}^T\mathbf{z} + c, \quad \mathbf{C} = \mathbf{A} + \lambda\mathbf{B},$$

where $\mathbf{b}$ is $\mathbf{b}_r$, $\mathbf{b}_l$ or $\mathbf{b}_t$, and $\mathbf{A}$ is $\mathbf{A}_r$, $\mathbf{A}_l$ or $\mathbf{A}_t$ as long as it is consistent with the form of $\mathbf{b}$. It can be shown [11] that although matrices $\mathbf{A}$ and $\mathbf{B}$ are symmetric positive semi-definite, $\mathbf{C}$ is usually symmetric positive definite. Then the minimization problem is equivalent to the solution of the linear system of equations

$$\mathbf{C}\mathbf{z} = \mathbf{b}.$$

Efficient iterative linear system solvers such as multi-grid method, PCG (Preconditioned Conjugate Gradient) method can be applied fot its solution.

To obtain more accurate reconstructed surface, a successive linearization scheme is applied to the reflectance map. That is, we linearize the reflectance map with respect to the local gradient point of the triangular patch obtained from the previous iteration, and perform the above solution procedure repeatedly.

4 Characteristics of the Reflectance Map

The single-image SFS algorithm discussed above has its limitation even if the exact lighting condition and surface reflectivity are known. One extreme case is that the 3-D surface information is totally lost under a certain lighting condition so that there is no way to recover the surface orientation due to the lack of information. This phenomenon can be illustrated by a simple example. Fig. 3(a) shows a 3-D height plot of a roof surface consisting of two planes which have slopes of the same magnitude but different signs. Figs. 3(b) and (c) are the synthesized images of Fig. 3(a) based on (2.1) and (2.3) with illuminating directions (tilt, slant) = $(0°, 45°)$ and $(90°, 45°)$, respectively. Since there is no intensity change in Fig. 3(b), it is natural to conclude that the surface is a plane from this image. In contrast, Fig. 3(c) contains enough information with which we are able to perform the exact 3-D shape reconstruction.

Since the SFS algorithm is an inverse process which recovers the surface orientations from the image irradiance through the reflectance map, the characteristics of the reflectance map play an important role in this problem. For simplicity, let us fix the value of $q = q_0$ and view the reflectance map $R(p, q_0)$ as a function of one variable p. The corresponding irradiance equation becomes

$$E = R(p, q_0). \tag{4.1}$$

The sensitivity of p with respect to the change in E can be estimated via

$$\left|\frac{\Delta p}{\Delta E}\right| = \left|\left(\frac{\partial R(p, q_0)}{\partial p}\right)^{-1}\right|, \tag{4.2a}$$

which is inversely proportional to the slope of the reflectance map at point p. Thus, for a fixed value of ΔE, the estimate $\hat{p}$ is more accurate (i.e. smaller value of Δp) for the region where $R(p, q_0)$ is steeper. Similar arguments can be made along the q-direction, i.e.

$$\left|\frac{\Delta q}{\Delta E}\right| = \left|\left(\frac{\partial R(p_0, q)}{\partial q}\right)^{-1}\right|. \tag{4.2b}$$

The contour plots of two typical reflectance maps are given in Figs. 4(a) and (b). They are skewed along the line passing through $(0, 0)$ and (p_s, q_s). If the spacings between the adjacent contour lines are narrower (or wider), the slopes of the reflectance map $R(p, q)$ are steeper (or smoother), or equivalently, the partial derivatives $R_p(p, q)$ and $R_q(p, q)$ of the reflectance map have larger (or smaller) absolute values. For a given point (p_0, q_0) in the gradient space, the sensitivity defined in (4.2) is highest along the gradient direction, i.e.

$$\nabla R(p_0, q_0) = (R_p(p_0, q_0), R_q(p_0, q_0)),$$

and lowest along the tangential direction, i.e. $(-R_q(p_0, q_0), R_p(p_0, q_0))$.

In practice, real images contain noises such as the sensor or quantization noises. Besides, the irradiance values are averaged to obtain a uniform brightness value for each triangular patch for the algorithm in Section 3. The averaging corresponds to a linear interpolation for the nonlinear reflectance map, which results in a modeling error. Since the image is corrupted by these noises, it is relatively difficult to obtain accurate surface orientations or heights in the region where the slope of the reflectance map is smooth. Furthermore, the components of the stiffness matrix are determined primarily by the partial derivatives of the reflectance map with respect to p and q as given by (3.4) and (3.8). Small values of α or β cause some elements of the stiffness matrix to be nearly zero and make the problem ill-conditioned so that the height or orientation related to those elements can not be easily determined. We observe that smaller values of the partial derivatives $R_p(p, q)$ and $R_q(p, q)$ often slow down the convergence rate of the iteration with successive linearization. The slow convergence behavior is clearly attributed to the large condition number of the original nonlinear minimization problem (3.6).

The following example is used to illustrate the above discussion. We plot in Figs. 5(a), (b) and (c) the original heights of a portion of a sphere, its corresponding distribution of the gradients (p, q) of the triangular surface patches and the synthesized image from the illumination direction (tilt, slant) = $(45°, 45°)$ with albedo = 250. We show the reconstructed surfaces, its corresponding (p, q) plot after 1 iteration in Figs. 6(a)-(b) and after 20 successive iterations in Figs. 6 (c)-(d). The (p, q) value of all points is set to zero initially. By comparing the (p, q) distributions in Fig 6(b) and (d) to the original one in Fig. 5(b), we can easily see that the gradient points spread quickly along the steepest descent direction of the reflectance map, and reach quite accurate values in one iteration. In contrast, the gradient points move slowly along the tangential direction of the contour lines and have not yet reached satisfying values even in 20 iterations.

5 Two Photometric Stereo SFS Algorithms

To overcome the difficulties resulted from a single reflectance map, it is natural to use several images taken under the different illumination directions while holding the same viewing direction. The photometric stereo images provide several reflectance map functions, which can be used to enhance the sensitivity of Δp and Δq with respect to ΔE over the gradient domain of our interest.

Given J different photometric stereo images E_{oj} with their corresponding reflectance maps $R_j(p,q)$, $j = 1, \ldots, J$, we consider two different schemes to combine them, namely, the parallel and cascade schemes. The parallel scheme is to use all images at the same time, and formulate all $R_j(p,q)$, $1 \leq j \leq J$, in one cost functional,

$$\mathcal{E} = \iint_{\Omega} \sum_{j=1}^{J} (E_{oj} - E_j)^2 \, dx \, dy + \frac{\lambda}{2} \iint (z_{xx}^2 + 2z_{xy}^2 + z_{yy}^2) \, dx \, dy, \tag{5.1}$$

where E_{oj} and E_j are the jth observed and parameterized images, respectively. By using the triangular element surface model and the linearized reflectance model, we can express (5.1) in the discrete form,

$$\mathcal{E} = \frac{1}{2} \mathbf{z}^T \tilde{\mathbf{C}} \mathbf{z} - \tilde{\mathbf{b}}^T \mathbf{z} + c, \quad \tilde{\mathbf{C}} = \tilde{\mathbf{A}} + \lambda \mathbf{B}, \tag{5.2}$$

where the overall stiffness matrix $\tilde{\mathbf{A}}$ and the load vector $\tilde{\mathbf{b}}$ are the sum of each individual stiffness matrix $\mathbf{A}_j$ and the load vector $\mathbf{b}_j$, i.e.

$$\tilde{\mathbf{A}} = \sum_{j=1}^{J} \mathbf{A}_j, \qquad \tilde{\mathbf{b}} = \sum_{j=1}^{J} \mathbf{b}_j. \tag{5.3}$$

More generally, we may choose different weighting coefficients for different images in (5.3) if appropriate. The nodal height vector $\mathbf{z}$ is the vector which minimizes the quadratic functional (5.2) and can be obtained by solving the linear system of equations,

$$\tilde{\mathbf{C}} \mathbf{z} = \tilde{\mathbf{b}}. \tag{5.4}$$

In contrast, the cascade scheme uses the photometric stereo images one after another in a cascade manner. The single-image SFS algorithm is used for each image and the previous result is used as the initial condition.

6 The Optimal lighting Conditions

To improve the performance of the single-image SFS algorithm, we incorporate reflectance maps that compensate each other's weakness. We know from Section 2 that

$$p_s = -\frac{\cos\tau \sin\sigma}{\cos\sigma},$$

and

$$q_s = -\frac{\sin\tau \sin\sigma}{\cos\sigma}.$$

Thus, the angle θ which the line passing through $(0,0)$ and (p_s, q_s) makes with the p-axis and the distance d between $(0,0)$ and (p_s, q_s) can be written as

$$\theta = \arctan\left(\frac{q_s}{p_s}\right) = \arctan(\tan\tau) = \tau,$$

and

$$d = \sqrt{p_s^2 + q_s^2} = \tan\sigma,$$

respectively. Note that the angle θ is exactly the same as the tilt angle τ, and the distance d depends only on the slant angle σ. Therefore, the tilt angle determines the orientation of the reflectance map around the origin whereas the slant angle determines the distance between the origin and (p_s, q_s) in the gradient space as well as the shape of the reflectance map. The angle between the two gradient directions of the reflectance maps with tilt angles τ_1 and τ_2 is simply $\mid \tau_1 - \tau_2 \mid$.

If the slant angle is in the range between 30° and 60°, the reflectance map covers the central region of the gradient space which is our main concern and has appropriate values in steepness. Thus, the optimal lighting condition is primarily dependent on the tilt angles of different light sources and not sensitive to the slant angles as long as they are between 30° and 60°. We know from the discussion in Section 4 that the reflectance map provides good sensitivity along the gradient direction but poor sensitively along the tangential direction. Consider two photometric stereo images illuminated from the same slant angle but different tilt angles. It is ideal that the gradient directions of one reflectance map correspond to the tangential directions of the other reflectance map over the region of our interest. This can be achieved by choosing the difference of their tilt angles to be 90°. One such example is given by Fig. 4(c), where the contour plots of two reflectance maps are shown together. The tilt angles are 45° and 135°, respectively while the slant angle (= 45°) and albedo

(= 250) are fixed. Note that the gradients of a smooth surface are usually concentrated on the central region of the gradient space, say, $-0.5 < p, q < 0.5$. It is clear from these two figures that the gradient direction of one reflectance map is the tangential direction of the other and vice versa in this region. To summarize, the optimal lighting condition can be written as

$$| \tau_1 - \tau_2 | = 90^\circ. \tag{6.1}$$

The condition (4.1b) can be verified by the experimental results shown in Table 1. The test object is the sombrero surface shown in Fig. 7(a). The rms error of the reconstructed surface height by the parallel and cascade schemes with varying tilt angles $(= 0^\circ, 15^\circ, \ldots, 345^\circ)$ while keeping slant angle $(= 45^\circ)$ and albedo (= 250). We see from these data that the parallel scheme produces more accurate reconstructed surface and the best result is obtained when the tilt angles of the two photometric stereo images are orthogonal to each other. That is, when the tilt angle of the second image is around 135° or 315° in this example. The error becomes larger when the two images are illuminated from similar tilt angles.

7 Experimental Results

Our algorithms have been applied to four sets of photometric stereo images. The first two sets (sombrero and Mozart) are synthetic images while the last two sets (faces of two statues) are real images. For each test problem, both parallel and cascade schemes are performed. The results are compared to those obtained from the single-image SFS algorithm described in [17]. We have also tested different illuminating directions with varying tilt angles for the sombrero image.

Test Problem 1: Sombrero

The tested photometric stereo images are generated from the sombrero surface as shown in Fig. 7(a). The corresponding (p, q) distribution is given in 7(b). The two photometric stereo images are generated by illuminating from (tilt, slant) = $(45^\circ, 45^\circ)$ and $(135^\circ, 45^\circ)$, respectively, with albedo = 250. They are shown in Figs. 7(c) and (d). Note that these two images are shaded by light sources with orthogonal tilt angles.

Results of the single-image SFS algorithm applied to Figs. 7(c) and (d) are given in Fig. 8. The results are not good in some regions. It is easier to see the discrepancies in the

Table 1: The rms error of the reconstructed surface height according to the variation of tilt angle of the second image for the parallel and the cascade schemes, (tilt, slant) = (45°, 45°) are fixed for the first image and slant = 45° are fixed for the second image.

tilt(°)	parallel	cascade
0	0.125186	0.187297
15	0.128692	0.231566
30	0.192990	0.360646
45	0.447816	0.431678
60	0.181018	0.336983
75	0.109999	0.218857
90	0.093384	0.208685
105	0.087438	0.226707
120	0.085450	0.221273
135	0.076186	0.237868
150	0.079959	0.225893
165	0.084040	0.210219
180	0.132937	0.186983
195	0.170376	0.201333
210	0.170710	0.261275
225	0.168250	0.347342
240	0.149476	0.299825
255	0.121514	0.217509
270	0.090110	0.192800
285	0.085979	0.204031
300	0.096235	0.210975
315	0.078121	0.214341
330	0.080660	0.212522
345	0.099063	0.214217

(p, q) domain. By comparing the distributions of these (p, q) values with the original one, we see clearly that points move slowly along the tangential directions of the contours. The results of the parallel and cascade schemes are shown in Fig. 9. For the cascade scheme, we first reconstruct the surface from the image given in Fig. 7(c) and then use it as the initial guess for another surface reconstruction algorithm based on the image in Fig. 7(d). By comparing the (p, q) distributions of the parallel scheme and the single-image method with that of the original one, we see that a significant improvement has been achieved by using the parallel scheme. This is due to that the two reflectance maps help each other and provide good sensitivity over the interested region of the gradient space as discussed in Sections 4 and 6. The cascade scheme provides a better result over the single-image SFS algorithm, but performs slightly worse than the parallel scheme as shown in Table 1. We conclude from this table that the parallel scheme produces more accurate surfaces, and the best result is achieved when the tilt angles are orthogonal to each other.

Test Problem 2: Mozart

The test images are synthesized from the Mozart statue, and the surface height is obtained from the range data. The original 3-D surface height is plotted in Fig. 10(a), and two images generated with illuminating directions (tilt, slant) = $(135°, 45°)$ and $(45°, 45°)$ and albedo = 250 are shown in Figs. 10(b) and (c). Note that there exist some defects in the original data such as points along the object boundaries and under the nose. The reconstructed surface heights are presented in Fig. 11. Figs. 11(a) and (b) show the 3-D plots of the reconstructed surfaces by the single-image SFS algorithm applied to images in Figs. 10(b) and (c), respectively. The results of the parallel and cascade schemes are shown in Figs. 11(c) and (d).

The reconstructed surfaces from the single-image SFS algorithm contain errors in regions over the face and background depending on the illumination direction, or equivalently, the reflectance map. In contrast, the reconstructed surface with the parallel scheme in Fig 11(c) is almost the same as the original one except at the discontinuities along the boundary and some defect points of the original surface. The reconstructed surface of the cascade scheme is not quite satisfactory. However, it is better than those obtained with the single-image SFS algorithm, which is consistent with the results in Test Problem 1.

Test Problem 3: Face of the David statue

The tested images are 128×128 real images of the statue of David's head illuminated from directions (tilt, slant) = (135°, 45°) and (45°, 45°) as shown in Figs. 12(a) and (b), respectively. Even though the plaster statue has a Lambertian surface, we would like to comment several problems concerning these images. First, it is difficult to get an ideal lighting condition satisfying the reflectance map model and, therefore, the observed brightness at a point may have undesirable distortions or variations due to the finite distance of the light source as well as the quantization noises. Second, the self-shadow problem often appears in real images. Since no shading information is available in self-shadowed regions, it is difficult to extract the correct shape information in those regions. Additional information such as shading from different illumination directions or other high level visual cues is often needed to recover the shape in the self-shadowed region. Note that although there exist self-shadow regions under the nose in both test images, they do not overlap with each other and hence provide sufficient information for surface reconstruction.

The results of the single-image SFS algorithm based on Figs. 12(a) and (b), and those of the parallel and cascade schemes are shown in Figs. 13 (a)-(d), respectively. By comparing the two reconstructed surfaces of the single-image SFS algorithm in Fig. 13(a) and (b), one can observe that they are not consistent with each other in several regions. Besides, the surface in Fig. 13(a) seems to be erroneous due to the ambiguity occurring in the cheek region as given in Fig. 12 (a). The reconstructed surface orientations are quite different from their true values, even though the brightness error is small. This phenomenon can be understood by examining the roof surface example in Fig. 3. A great deal of improvement has been achieved by the parallel scheme, and the result in Fig. 13 (c) looks very nice. Both brightness distortion effect and self-shadow problems are clearly minimized by combining photometric stereo images. The reconstructed surface in Fig. 13(d) is obtained by the cascade scheme, where the result of Fig. 13(b) is used as the initial height for surface reconstruction based on the image of Fig. 12(a). We see that the ambiguity in Fig. 12(a) is eliminated due to a proper initial guess.

Test Problem 4: Face of the Agrippa statue

The test images are 128 × 128 real images of the Agrippa statue as shown in Figs. 14(a) and (b) where the estimated illumination directions are (tilt, slant) = (135°, 50°) and (45°, 45°), respectively. These images have relatively large regions of self-shadow. The results of the single-image SFS algorithm and the parallel and cascade schemes are shown in Figs. 15 (a)-(d). We observe from Figs. 15(a) and (b) that ambiguities, which are similar to that discussed in the previous test problem, occur for both surfaces in several regions including cheeks. Moreover, the self-shadow problem is quite serious. It is evident from Figs. 15(c) and (d) that both ambiguity and self-shadow problems are resolved by using photometric stereo SFS schemes and, in particular, by using the parallel scheme. Note also that the two images in Figs. 14(a) and (b) have common self-shadowed regions near the eyes. The reconstructed shape of the regions may not be accurate since no sufficient shading information is provided. This situation often happens in practice and may be handled by incorporating additional photometric stereo image which gives shading information in these regions.

8 Conclusion and Extension

We have shown that the accuracy of the reconstructed surface and the performance of the single-image SFS algorithm are highly related to the slop of the reflectance map function in the gradient space. Based on this observation, we proposed two new iterative SFS algorithms, i.e. parallel and cascade schemes, using multiple photometric stereo images taken under different lighting conditions. More accurate surfaces can be reconstructed by combining several reflectance maps and the corresponding image information together. Based on the linear approximation of the reflectance map and a triangular element surface model, these two schemes are formulated as a quadratic functional minimization problem parametrized by surface heights, where the cost functional is given by the squares of the brightness error obtained from each individual image in a parallel or cascade manner. Surface heights are obtained directly by solving the equivalent large linear system of equations with efficient linear system solvers such as the MG (Multi-Grid) or the PCG (Preconditioned Conjugate Gradient) method. These methods do not require any additional integrability constraint or artificial boundary assumption.

Our algorithms are tested on several images. Experimental results show that both schemes produce more accurate reconstructed surface compared to the single-image SFS algorithm. Especially, it is shown that the parallel scheme is robust and reliable, and gives accurate results for all test problems. The effect of different illumination directions of two light sources is also tested. We conclude that the best result can be obtained when the two illumination directions are orthogonal to each other, since their reflectance maps complement each other in the optimal way in the central region of the (p, q) domain. Our proposed schemes work very well for synthetic images as well as real ones. Even in the presence of intensity distortions, noises and self-shadows in real images, the new photometric SFS schemes produce robust reconstructed surfaces, while the single-image SFS algorithm does not.

Compared to the conventional photometric stereo method, our new iterative SFS method has two major advantages: no integrability problem and being insensitive to the noise. However, our method requires the smooth surface assumption whereas the conventional method does not. It is interesting to see the combination of the conventional with the new method. For example, the application of the conventional method in regions with discontinuities and changing albedo while the application of the new method to the remaining region.

References

[1] R. Frankot and R. Chellappa, "A method for enforcing integrability in shape from shading algorithm," *IEEE Trans. Pattern Anal. Machine Intell.*, Vol. 10, No. 4, pp. 439–451, 1989. Also in *Shape from Shading*, B.K. P. Horn and M. J. Brooks (eds.) 1989, MIT Press, Cambridge, MA.

[2] B. Horn, *Shape from shading: a method for obtaining the shape of a smooth opaque object from one view*, Ph.D. dissertation, Massachusetts Institute of Technology, Cambridge, MA, 1970.

[3] B. Horn, *Obtaining Shape from Shading Information*, Cambridge, Massachusetts: The MIT Press, 1975.

[4] B. Horn, "Height and gradient from shading," A.I. Memo 1105, Massachesetts Institute of Technology, Cambridge, MA, 1989.

[5] B. Horn and M. Brooks, "The variational approach to shape from shading," *Computer Vision, Graphics, and Image Processing*, Vol. 33, pp. 174–208, Nov. 1986. Also in *Shape from Shading*, B.K. P. Horn and M. J. Brooks (eds.) 1989, MIT Press, Cambridge, MA.

[6] K. Ikeuchi, "Determining Surface Orientations of Specualr Surfaces by Using the Photometric Stereo Method," *IEEE Trans. Pattern Analysis and Machine Inteligence*, Vol. PAMI-13, pp. 661–669, November 1981.

[7] K. Ikeuchi and B. Horn, "Numerical shape from shading and occluding boundaries," *Artificial Intelligence*, Vol. 17, pp. 141–184, Aug. 1981. Also in *Shape from Shading*, B.K. P. Horn and M. J. Brooks (eds.) 1989, MIT Press, Cambridge, MA.

[8] C. Johnson, *Numerical Solutions of Partial Differential Equations by the Finite Element Method*, Cambridge: Cambridge University Press, 1987.

[9] E. C. Jr. and R. Jain, "Obtaining 3-dimensional shape of textured and specular surface using four-source photometry," *Computer Graphics and Image Processing*, Vol. 18, pp. 309–328, 1982.

[10] D. Lee, "A provably convergent algorithm for shape from shading," in *Shape from Shading* (B. Horn and M. Brooks, eds.), pp. 349–373, Cambridge, Massachusetts: The MIT Press, 1989.

[11] K. Lee and C.-C. J. Kuo, "Shape from Shading with a Linear Trinagular Element Surface Model," Tech. Rep. 172, USC, Signal and Image Processing Institute, 1991.

[12] R. C. M. Shao and T. Simchony, "Reconstructing a 3-D depth map from one or more images," *Computer Vision, Graphics, Image Processing: Image Understanding*, Vol. 53, pp. 219–226, March 1991.

[13] A. Pentland, "Shape information from shading: a theory about human perception," in *Proc. of International Cof. on Computer Vision*, pp. 404–413, 1988.

[14] J. B. R. Ray and R. kelly, "Error analysis of surface normals determined by radiometry," *IEEE Trans. Pattern Analysis and Machine Inteligence*, Vol. PAMI-5, pp. 631–645, Nov. 1983.

[15] H. Schwartz, *Finite Element Methods*, Academic Press, 1988.

[16] W. Silver, "Determining shape and reflectance using multiple images," Master's thesis, Massachusetts Institute of Technology, Cambridge, MA, 1980.

[17] G. Smith, "The relationship between image irradiance and surface orientation," in *IEEE Conference on Computer Vision and Pattern Recognition*, (Washington D.C.), pp. 404–413, June 1983.

[18] R. Szeliski, "Fast surface intrpolation using hierachical basis functions," *IEEE Trans. Pattern Analysis and Machine Inteligence*, Vol. PAMI-12, pp. 513–528, June 1990.

[19] R. Szeliski, "Fast shape from shading," *Computer Vision, Graphics, Image Processing : Image Understanding*, Vol. 53, pp. 129–153, March 1991.

[20] H. tagare and R. DeFigueiredo, "A theory of photometric stereo for a class of diffuse non- lambertian surface," *IEEE Trans. Pattern Analysis and Machine Inteligence*, Vol. PAMI-13, pp. 133–152, Feb. 1991.

[21] D. Terzopoulos, "Multilevel computational processes for visual surface reconstruction," *Computer Vision, Graphics, and Image Processing*, Vol. 24, pp. 52–96, 1983.

[22] D. Terzopoulos, "The computation of visual surface representation," *IEEE Trans. Pattern Analysis and Machine Inteligence*, Vol. PAMI-10, pp. 417–438, July 1988.

[23] R. Woodham, "A cooperative algorithm for determining surface orientation from a single view," in *Internal Joint Conference on Artificial Intelligence*, (Cambridge, MA), pp. 635–641, August 1977.

[24] R. Woodham, "Photometric method for determining surface orientation from multiple images," *Optical Engineering*, Vol. 19, pp. 139–144, January/February 1980.

[25] R. Woodham, "Analysing Images of Curved Surfaces," *Artificial Intelligence*, Vol. 17, pp. 117–140, August 1981.

[26] Q. Zheng and R. Chellappa, "Estimation of illumination direction, albedo, and shape from shading," *IEEE Trans. Pattern Analysis and Machine Inteligence*, Vol. PAMI-13, pp. 680–702, July 1991.

Figure Captions

Figure 1: A uniform triangulation of a square domain Ω.

Figure 2: A nodal basis function ϕ_i.

Figure 3: The example of a roof surface: (a) 3-D height plot; (b) and (c) are synthesized images with (albedo, tilt, slant) = $(230, 0^\circ, 45^\circ)$ and $(230, 90^\circ, 45^\circ)$, respectively.

Figure 4: Contour plots of two reflectance maps with (a) (albedo, tilt, slant) = $(250, 45^\circ, 45^\circ)$ or $(p_s, q_s) = (-0.707, -0.707)$ and (b) (albedo, tilt, slant) = $(250, 135^\circ, 45^\circ)$ or $(p_s, q_s) = (0.707, -0.707)$; (c) combined reflectance map of (a) and (b). .

Figure 5: The example of a sphere surface: (a) the ground truth; (b) (p, q) distribution in the gradient space; (c) synthesized image with (albedo, tilt, slant) = $(250, 45^\circ, 45^\circ)$.

Figure 6: Results of the single-image SFS algorithm applied to the sphere image in Fig. 5(c): (a) and (b) are the reconstructed height and the corresponding (p, q) plot after 1 iteration; (c) and (d) are the reconstructed height and the corresponding (p, q) plot after 20 successive iterations.

Figure 7: The sombrero test problem: (a) the ground truth of the sombrero surface; (b) (p, q) distribution in the gradient space, (c) synthesized image with (albedo, tilt, slant) = $(250, 45^\circ, 45^\circ)$; (d) synthesized image with (albedo, tilt, slant) = $(250, 135^\circ, 45^\circ)$.

Figure 8: Results of the single-image SFS algorithm applied to the sombrero images: (a) and (b) are the reconstructed height and the corresponding (p, q) plot based on the image of Figure 7(c); (c) and (d) are the reconstructed height and the corresponding (p, q) plot based on the image of Figure 7(d).

Figure 9: Results of the photometric stereo SFS algorithm applied to the sombrero images: (a) and (b) are the reconstructed height and the corresponding (p, q) plot by the parallel scheme; (c) and (d) are the reconstructed height and the corresponding (p, q) plot by the cascade scheme.

Figure 10: The Mozart test problem: (a) the ground truth of the Mozart statue; and two synthetic images illuminated with (b) (albedo, tilt, slant) = $(250, 135^\circ, 45^\circ)$ and (c) (albedo, tilt, slant) = $(250, 45^\circ, 45^\circ)$.

Figure 11: Results of the SFS algorithms applied to the Mozart images: (a) and (b) are the reconstructed heights from Fig. 10(a) and (b) by the single-image SFS algorithm; (c) and (d) are the reconstructed heights by the photometric stereo SFS algorithms with the parallel and cascade schemes, respectively.

Figure 12: The David test problem: two real images of the David statue illuminated with (a) (tilt, slant) = $(135^\circ, 45^\circ)$; (b) (tilt, slant) = $(45^\circ, 45^\circ)$.

Figure 13: Results of SFS algorithms applied to the David images: (a) and (b) are the reconstructed heights from Fig. 15(a) and (b) by the single-image SFS algorithm; (c) and (d) are the reconstructed heights by the photometric stereo SFS algorithms with the parallel and cascade schemes, respectively.

Figure 14: The Agrippa test problem: two real images of the Agrippa statue illuminated with (a) (tilt, slant) = $(135^\circ, 50^\circ)$; (b) (tilt, slant) = $(45^\circ, 45^\circ)$.

Figure 15: Results of SFS algorithms applied to the Agrippa images: (a) and (b) are the reconstructed heights from Fig. 17(a) and (b) by the single-image SFS algorithm; (c) and (d) are the reconstructed heights by the photometric stereo SFS algorithms with the parallel and cascade schemes, respectively.

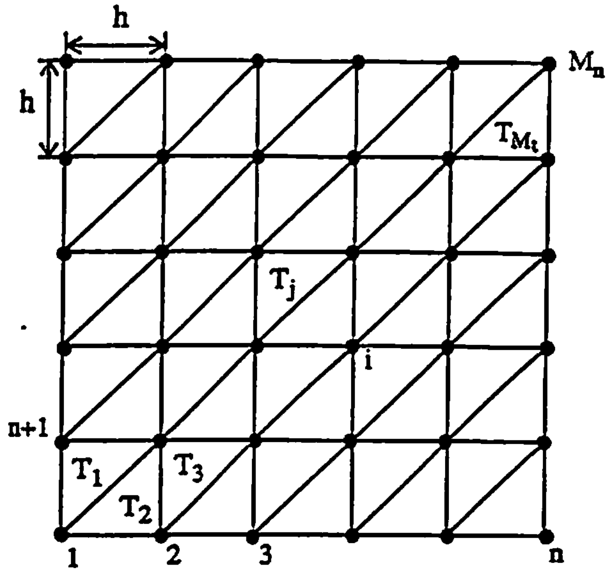

Fig. 1. A uniform triangulation of a square domain Ω.

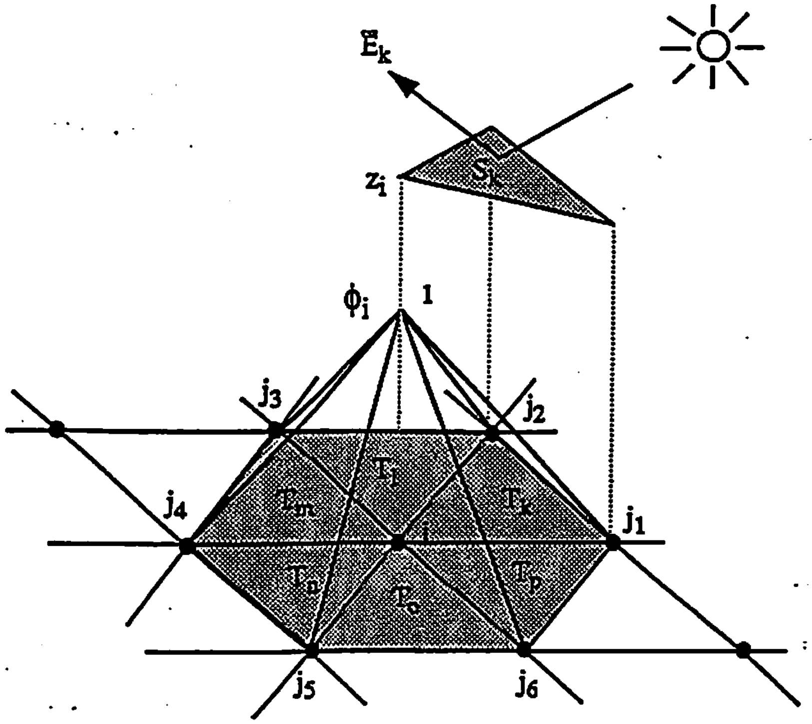

Fig. 2. A nodal basis function ϕ_i.

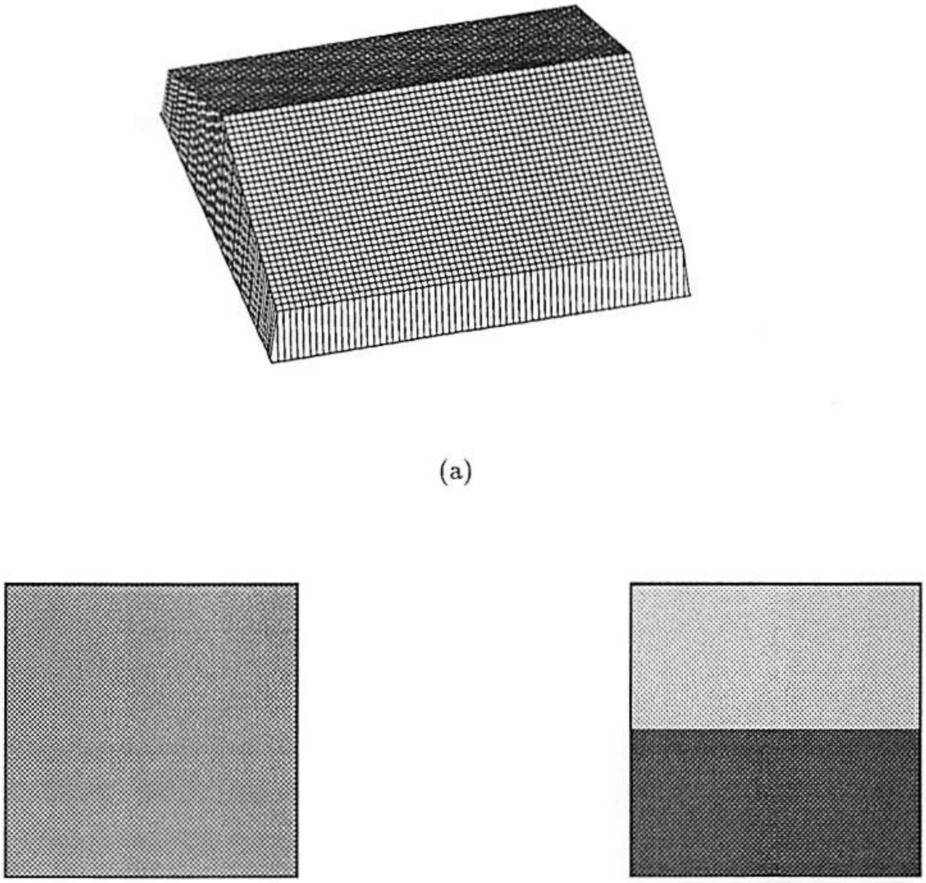

(a)

(b)

(c)

Figure 3: The example of a roof surface: (a) 3-D height plot; (b) and (c) are synthesized images with (albedo, tilt, slant) = $(230, 0°, 45°)$ and $(230, 90°, 45°)$, respectively.

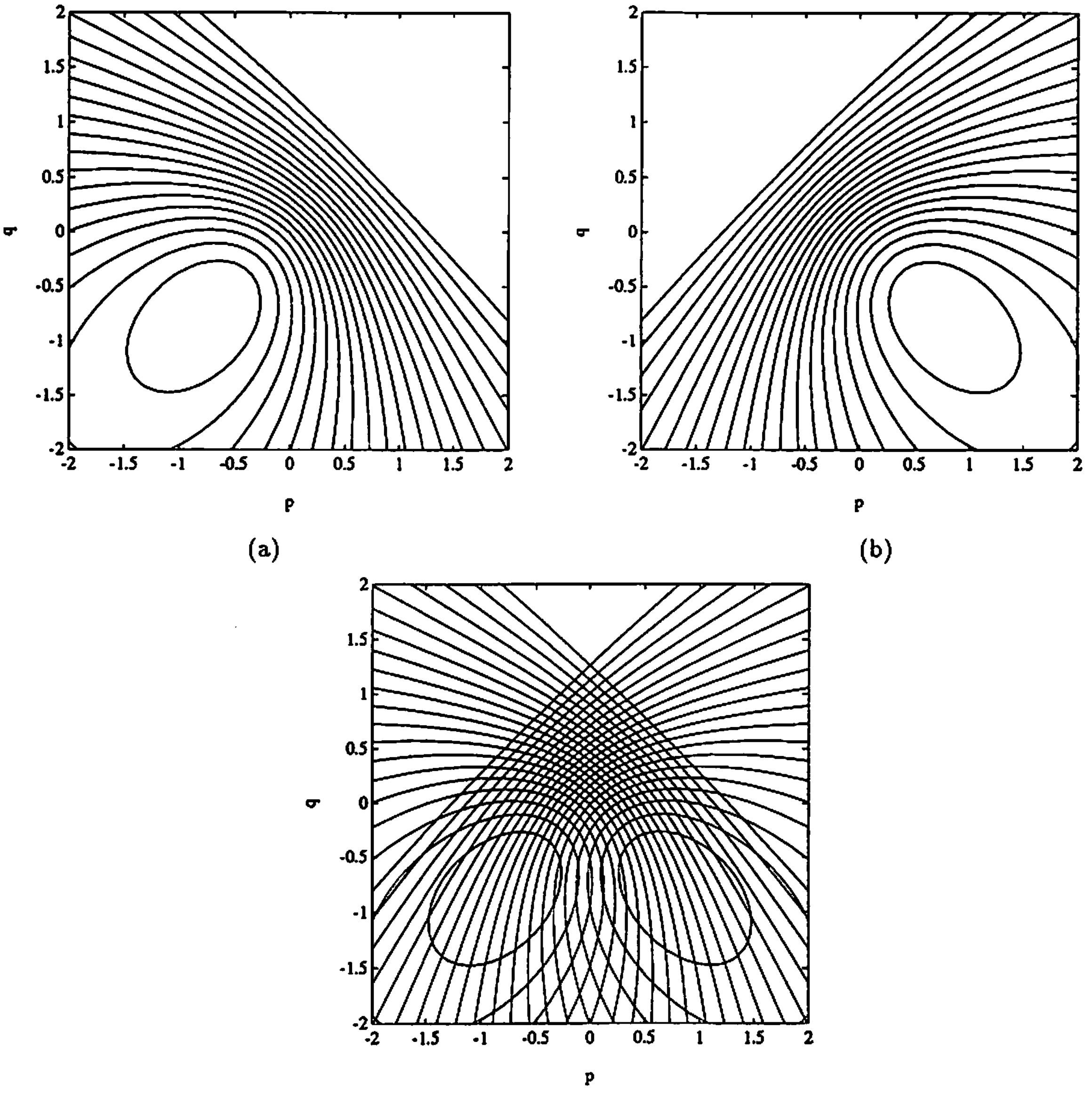

(a)

(b)

(c)

Figure 4: Contour plots of two reflectance maps with (a) (albedo, tilt, slant) = $(250, 45^\circ, 45^\circ)$ or $(p_s, q_s) = (-0.707, -0.707)$; (b) (albedo, tilt, slant) = $(250, 45^\circ, 45^\circ)$ or $(p_s, q_s) = (0.707, -0.707)$; (c) combined reflectance map of (a) and (b).

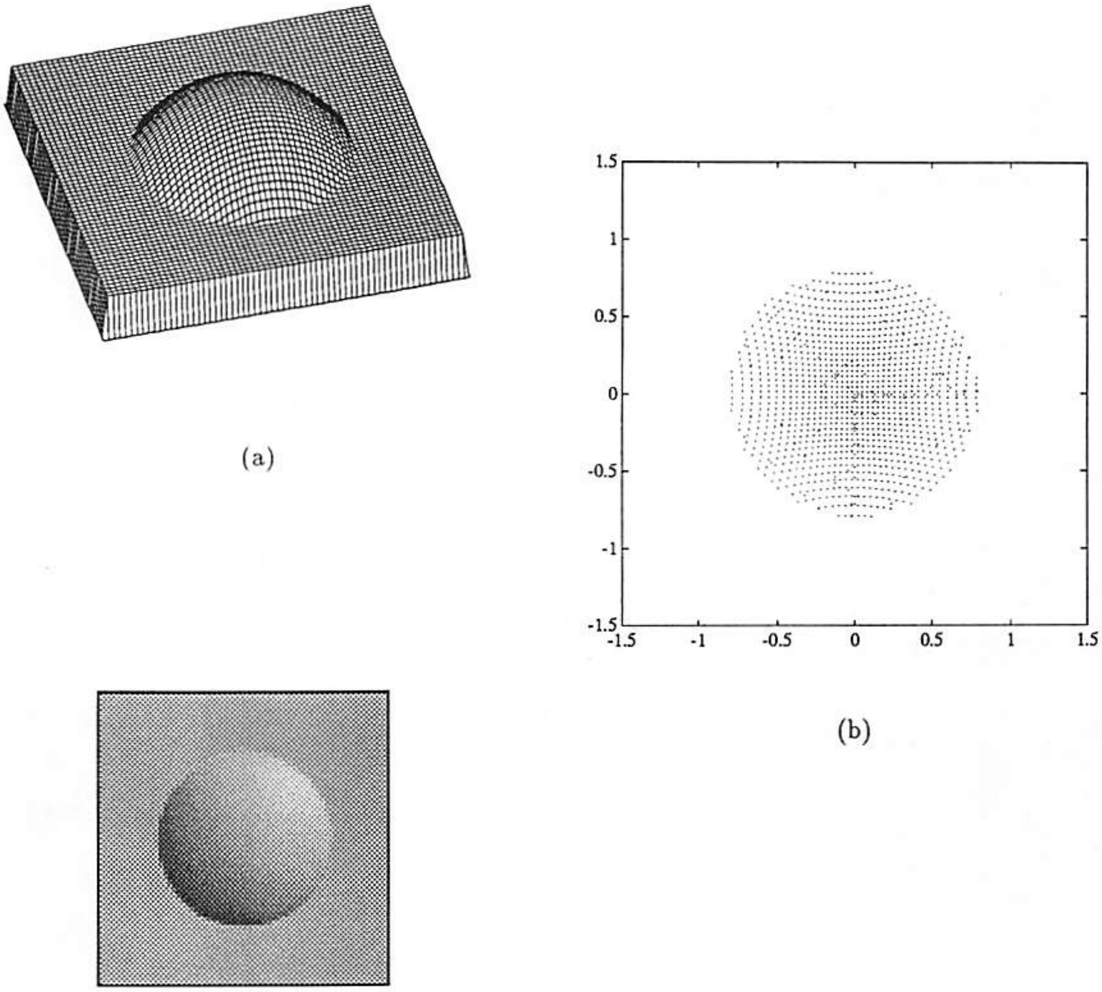

(a)

(b)

(c)

Figure 5: The example of a sphere surface: (a) the ground truth; (b) (p, q) distribution in the gradient space; (c) synthesized image with (albedo, tilt, slant) = $(250, 45°, 45°)$

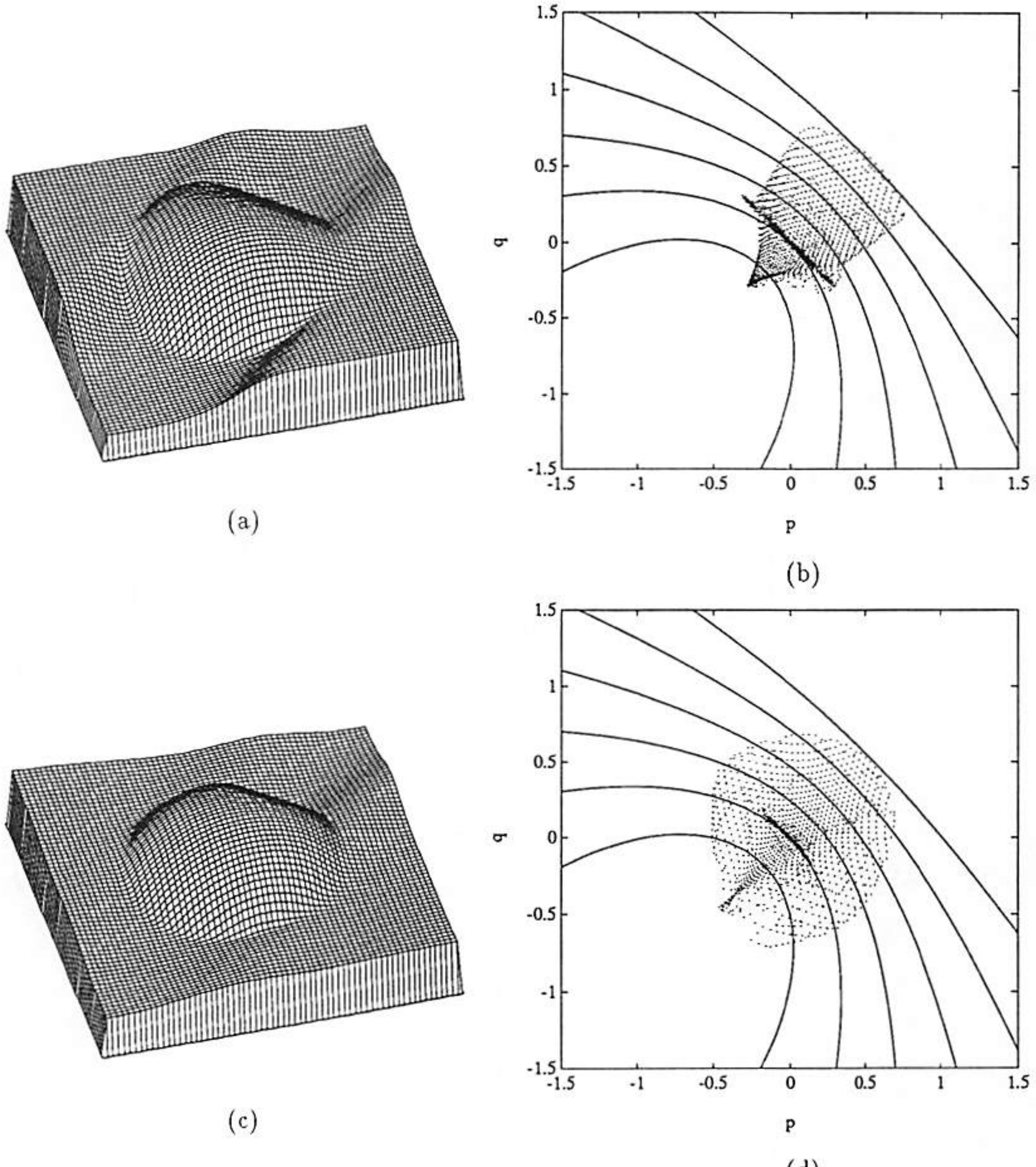

(a)

(b)

(c)

(d)

Figure 6: Results of the single-image SFS algorithm applied to the sphere image in Fig. 5(c): (a) and (b) are the reconstructed height and the corresponding (p, q) plot after 1 iteration; (c) and (d) are the reconstructed height and the corresponding (p, q) plot after 20 successive iterations.

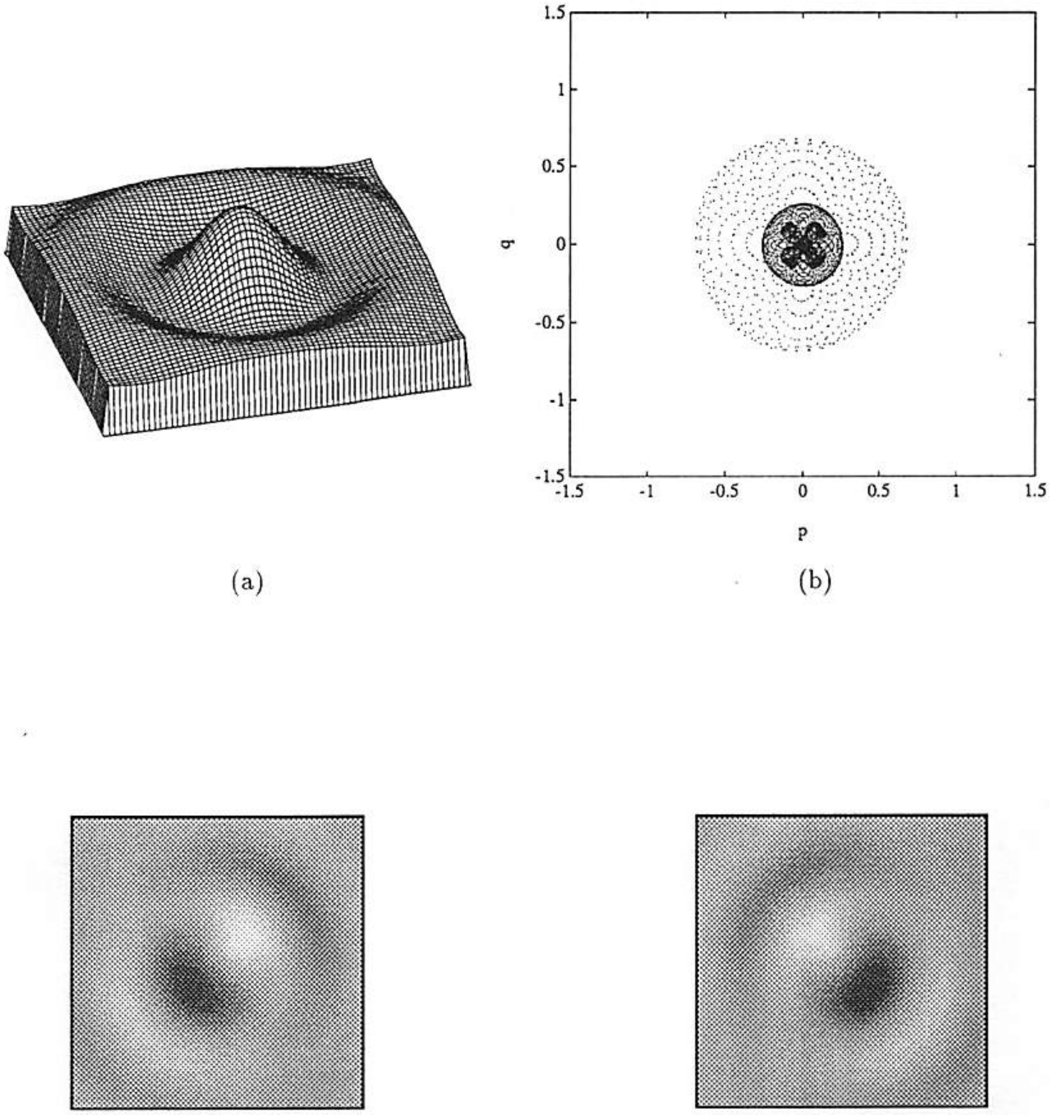

(a) (b)

(c) (d)

Figure 7: The sombrero test problem: (a) the ground truth of the sombrero surface; (b) (p, q) distribution in the gradient space, (c) synthesized image with (albedo, tilt, slant) = $(250, 45°, 45°)$; (d) synthesized image with (albedo, tilt, slant) = $(250, 135°, 45°)$.

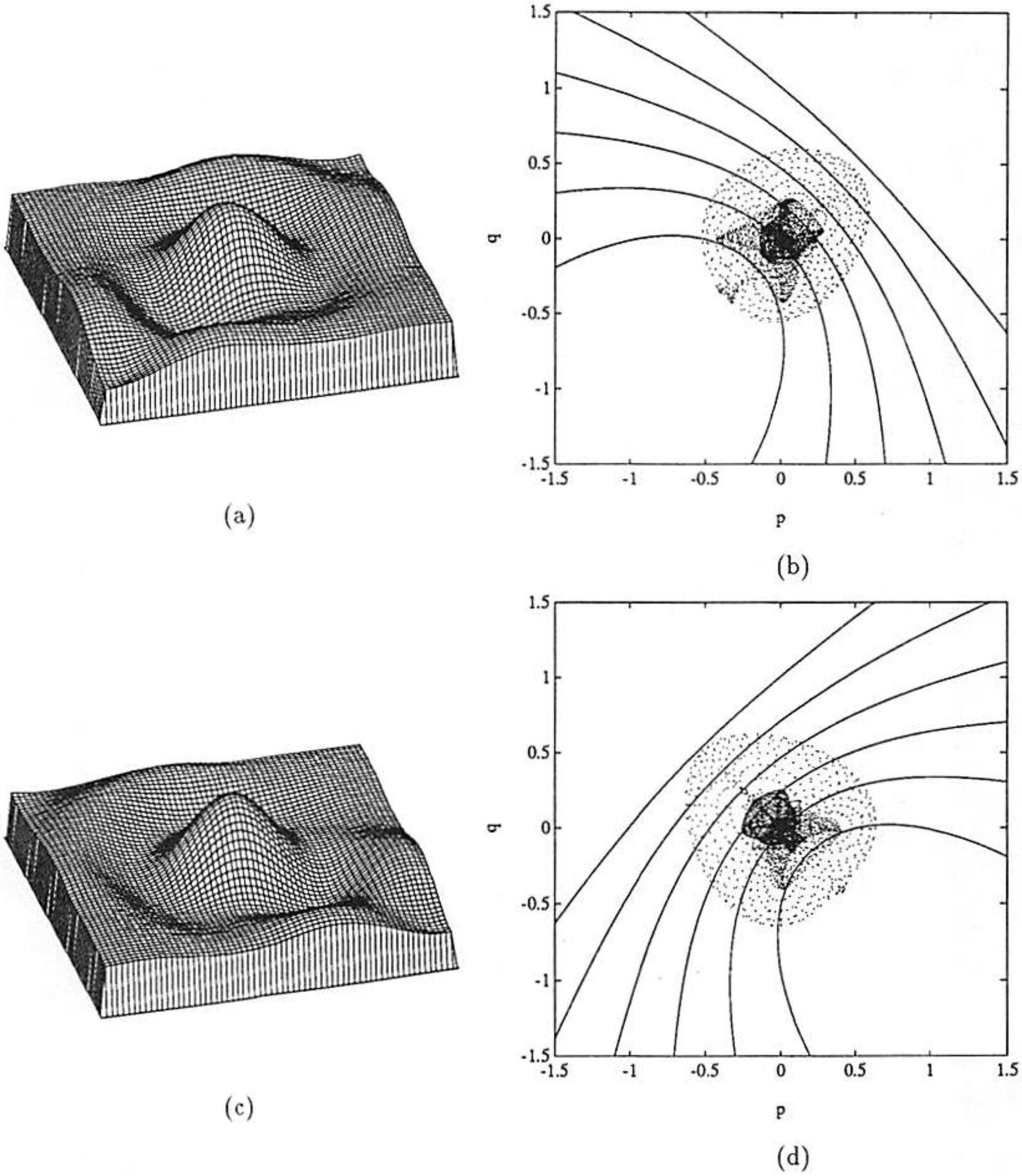

(a)

(b)

(c)

(d)

Figure 8: Results of the single-image SFS algorithm applied to the sombrero images: (a) and (b) are the reconstructed height and the corresponding (p, q) plot based on the image of Figure 7(c); (c) and (d) are the reconstructed height and the corresponding (p, q) plot based on the image of Figure 7(d).

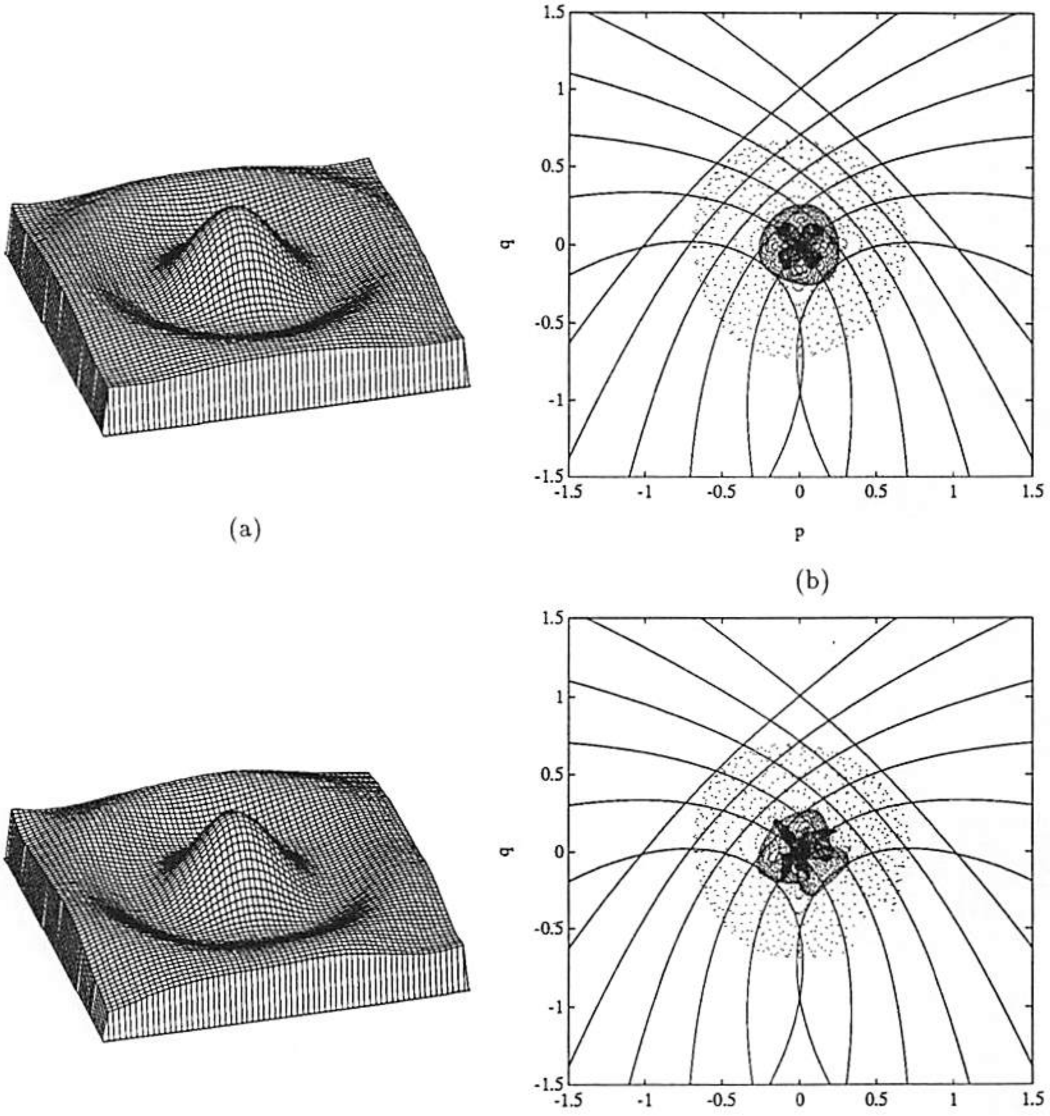

(a)

(b)

(c)

(d)

Figure 9: Results of the photometric stereo SFS algorithm applied to the sombrero images: (a) and (b) are the reconstructed height and the corresponding (p, q) plot by the parallel scheme; (c) and (d) are the reconstructed height and the corresponding (p, q) plot by the cascade scheme.

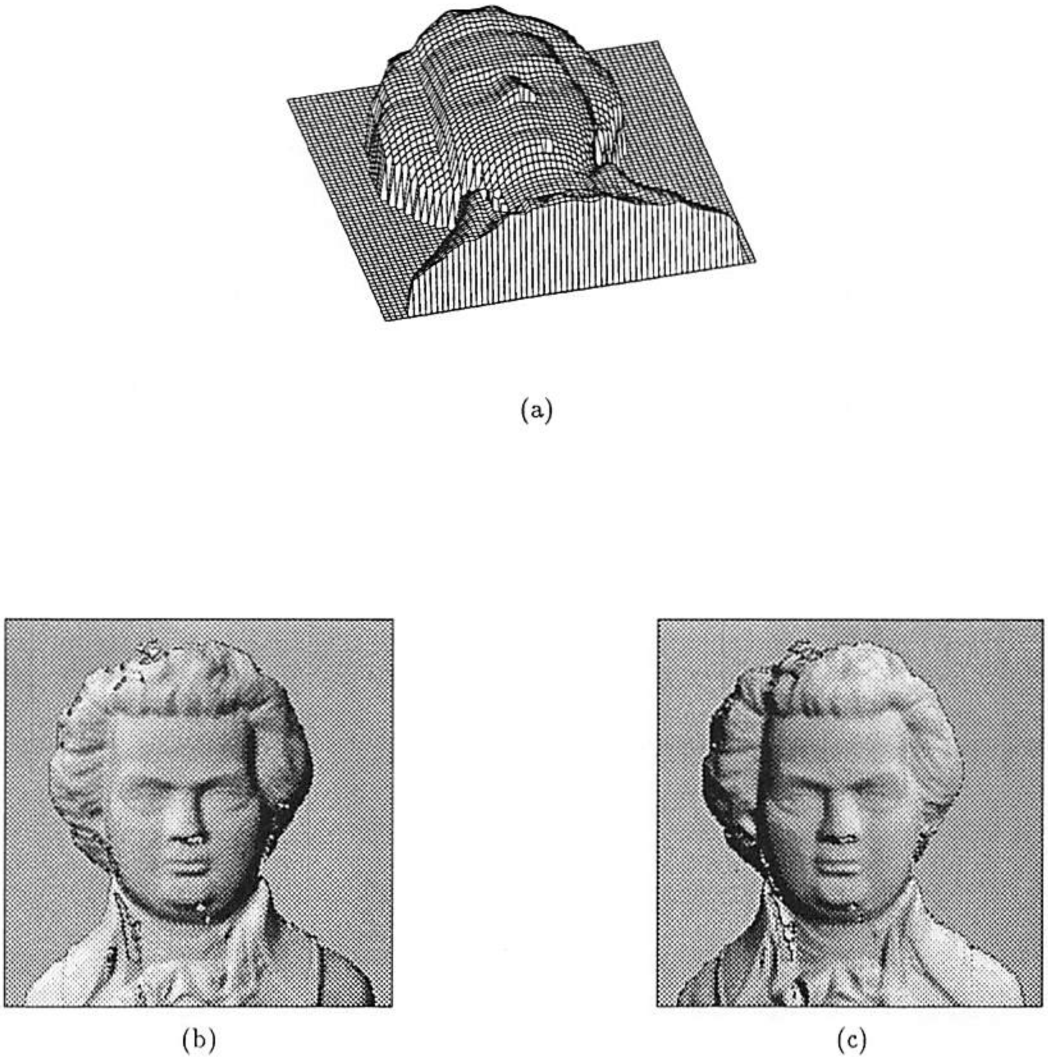

(a)

(b)

(c)

Figure 10: The Mozart test problem: (a) the ground truth of the Mozart statue; and two synthetic images illuminated with (b) (albedo, tilt, slant) = $(250, 135°, 45°)$ and (c) (albedo, tilt, slant) = $(250, 45°, 45°)$.

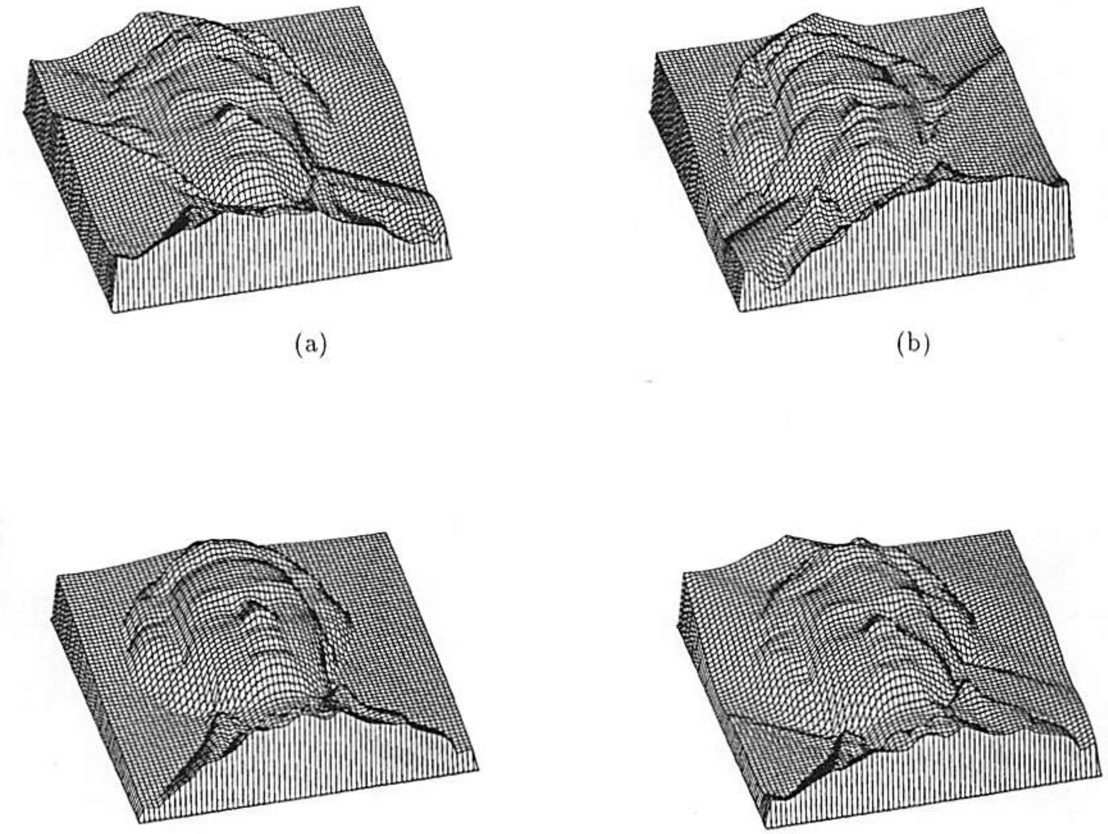

(a) (b)

(c) (d)

Figure 11: Results of the SFS algorithms applied to the Mozart images: (a) and (b) are the reconstructed heights from Fig. 10(a) and (b) by the single-image SFS algorithm; (c) and (d) are the reconstructed heights by the photometric stereo SFS algorithms with the parallel and cascade schemes, respectively.

(a) (b)

Figure 12: The David test problem: two real images of the David statue illuminated with (a) (tilt, slant) = $(135^\circ, 45^\circ)$; (b) (tilt, slant) = $(45^\circ, 45^\circ)$.

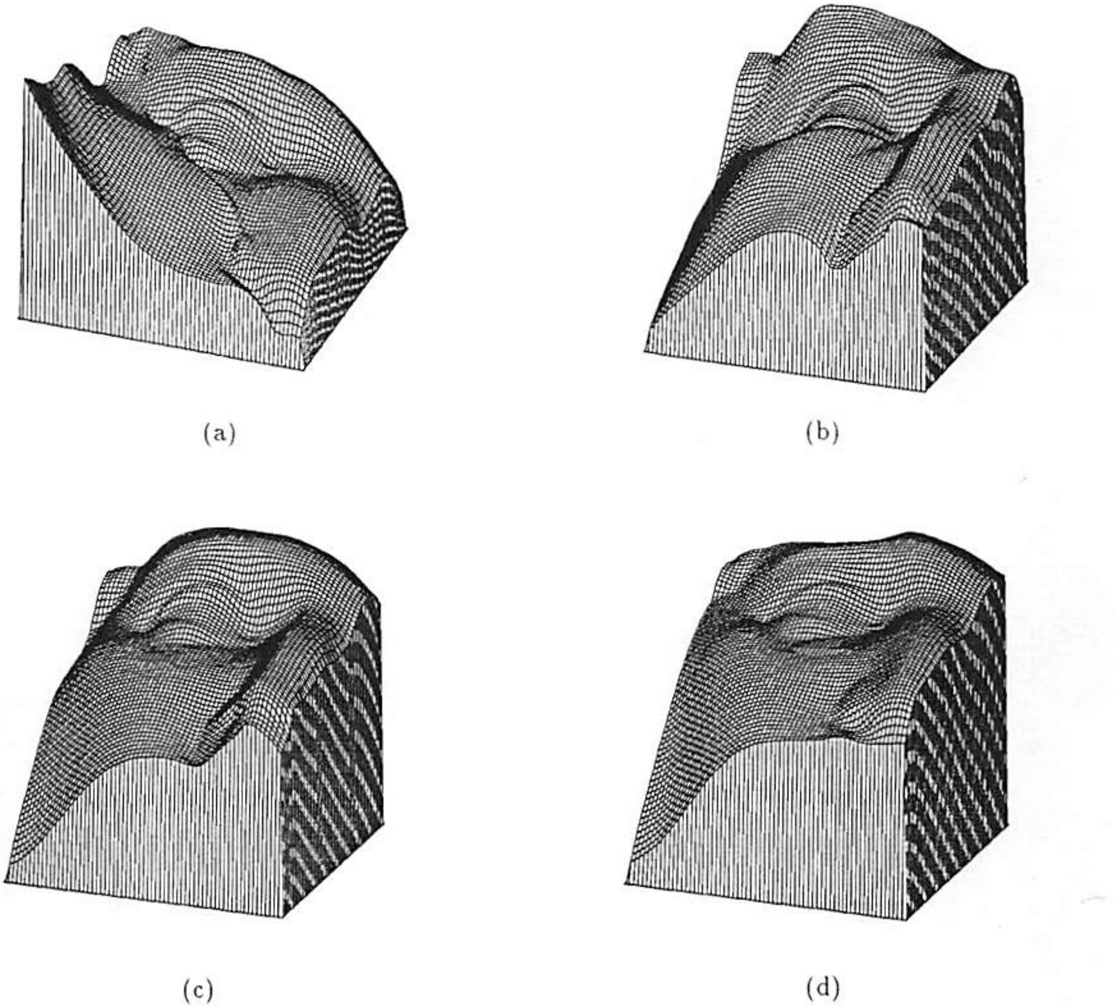

Figure 13: Results of SFS algorithms applied to the David images: (a) and (b) are the reconstructed heights from Fig. 15(a) and (b) by the single-image SFS algorithm; (c) and (d) are the reconstructed heights by the photometric stereo SFS algorithms with the parallel and cascade schemes, respectively.

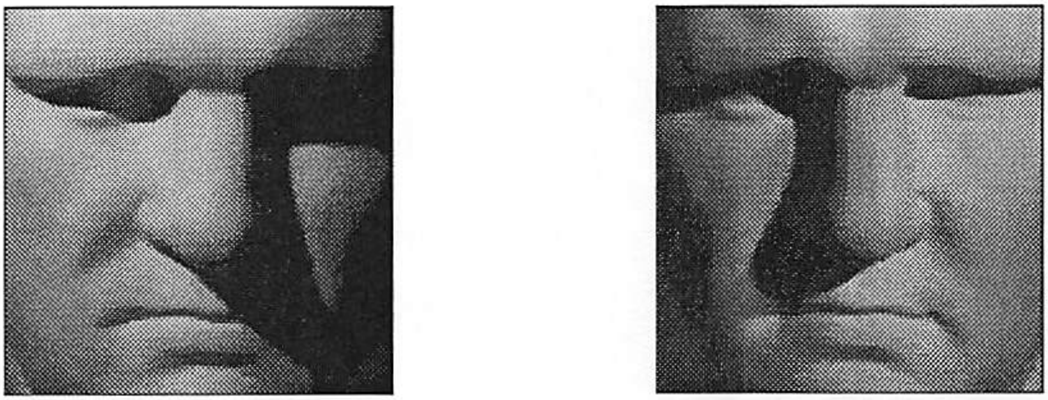

(a) (b)

Figure 14: The Agrippa test problem: two real images of the Agrippa statue illuminated with (a) (tilt, slant) = $(135°, 50°)$; (b) (tilt, slant) = $(45°, 45°)$.

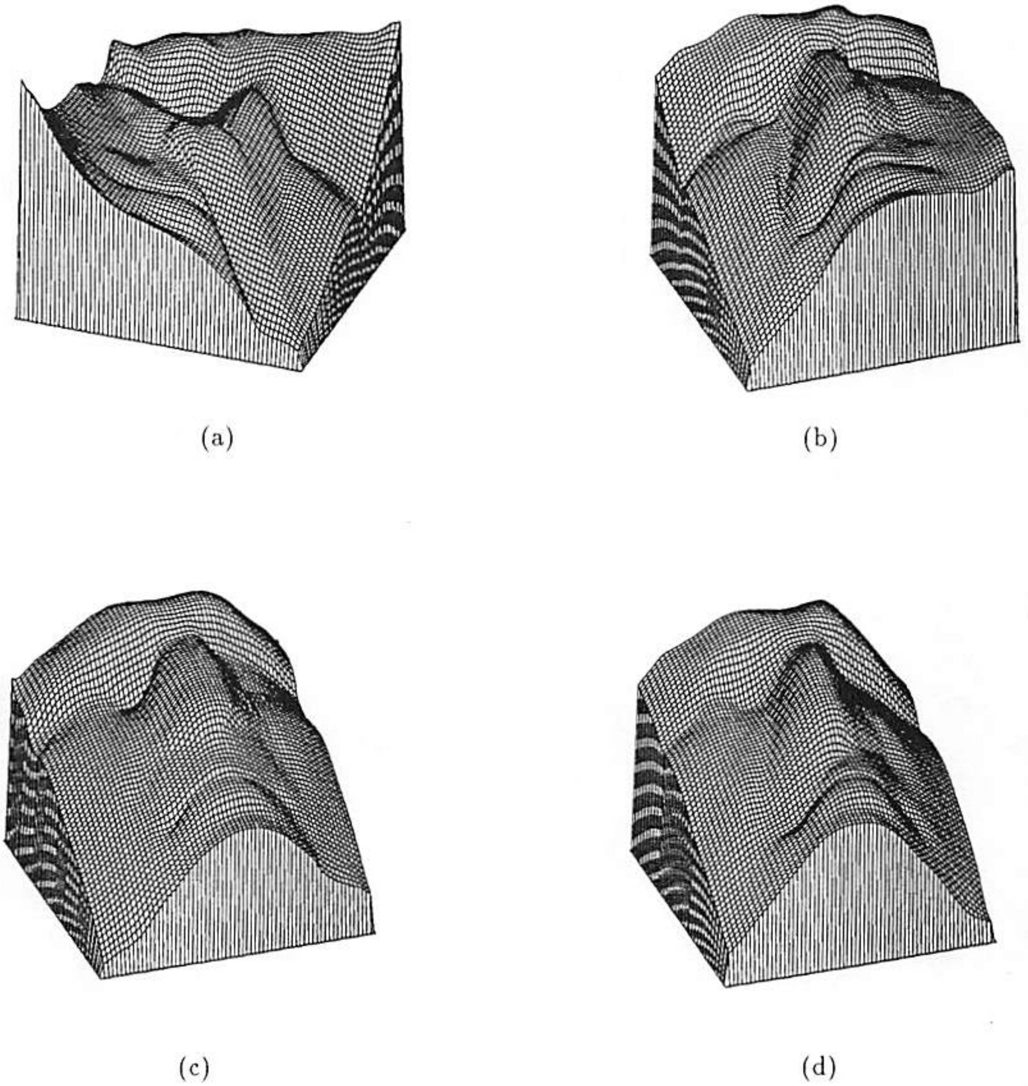

(a) (b)

(c) (d)

Figure 15: Results of SFS algorithms applied to the Agrippa images: (a) and (b) are the reconstructed heights from Fig. 17(a) and (b) by the single-image SFS algorithm; (c) and (d) are the reconstructed heights by the photometric stereo SFS algorithms with the parallel and cascade schemes, respectively.